metals

MDPI

Article

Study on σ Phase in Fe–Al–Cr Alloys

Jintao Wang [1,*], Shouping Liu [1] and Xiaoyu Han [2]

[1] College of Materials Science and Engineering, Chongqing University, Chongqing 400044, China; LSP@cqu.edu.cn
[2] Chongqing Materials Research Institute, Chongqing 400707, China; xiaoyuhan@cqu.edu.cn
* Correspondence: 201709131171@cqu.edu.cn; Tel.: +86-133-6406-1236

Received: 12 September 2019; Accepted: 9 October 2019; Published: 11 October 2019

Abstract: In this paper, a method of using the second phase to control the grain growth in Fe–Al–Cr alloys was proposed, in order to obtain better mechanical properties. In Fe–Al–Cr alloys, austenitic transformation occurs by adding austenitizing elements, leading to the formation of the second phase and segregation at the grain boundaries, which hinders grain growth. FeCr(σ) phase was obtained in the Fe–Al–Cr alloys, which had grains of several microns and was coherent and coplanar with the matrix (Fe_2AlCr). The nucleation of σ phase in Fe–Al–Cr alloy was controlled by the ratio of nickel to chromium. When the Ni/Cr (eq) ratio of alloys was more than 0.19, σ phase could nucleate in Fe–Al–Cr alloy. The relationship between austenitizing and nucleation of FeCr(σ) phase was given by thermodynamic calculation.

Keywords: high-aluminum steel; second phase; phase transition; thermodynamic calculation

1. Introduction

Heat-resistant ferritic steels have better heat capacity and a lower thermal expansion rate than nickel-based alloys. The growth rate and adhesion of Al-rich oxide film on Fe–Al–Cr alloy are not affected by water vapor because of its good thermal cycling resistance. Depending on the protective thermal growth oxides (TGO) to prolong the service life of alloys under harsh working conditions and maintain the stability of material systems and isolate pollutants, many researchers have proposed that Fe–Al–Cr alloys can be regarded as a new generation of nuclear fuel cladding materials [1,2]. The coarse grains are the main factor hindering the development of Fe–Al–Cr alloys. In recent years, researchers generally intend to use the second phase in Fe–Al–Cr alloys to refine the grains and strengthen the matrix. The (Ni, Fe) Al precipitates have been studied most [3–5]. C. Stallybrass et al. have suggested that the high temperature strength of nickel-based superalloys is attributed to the dispersion strengthening of Ni3Al. Similar microstructures could be obtained in the Fe–Al–Ni–Cr system with B2 ordered (Ni, Fe) Al precipitates in the ferritic matrix superalloys.

In the Fe–Cr–Al ternary system, there is a miscible zone between the disordered A2 phase and the ordered B2 phase [6]. These two phases have similar lattice parameters, and they are coherent and coplanar, which is a characteristic shared by alloys consisting of miscible phases and nickel-based superalloys. In general, the volume fraction of precipitates strengthened by coherent B2 (Ni, Fe) Al precipitates is 13% and the average precipitation radius is 62 nm [7]. The creep mechanism is the repulsive elastic interaction between the general dislocation climb, the coherent precipitate, and the matrix dislocation [8–12].

However, the Ni–Al phase plays an important role in precipitation strengthening and does not fundamentally refine the grain size of Fe–Al–Cr alloys. The aim of this study was to limit the grain growth of Fe–Al–Cr alloys by searching for a continuous and inhomogeneous micron-sized second phase in order to achieve good mechanical properties. FeCr has entered our field of vision, because it has a body-centered cubic lattice similar to ferrite, its crystal group is Im3m (229), and it is easy to nucleate at the grain boundary. As a common second phase in nickel-based superalloys, we tried to study its effects on iron-based superalloys.

2. Experimental Procedures

Four alloys with different chemical compositions (Table 1) were melted in a vacuum induction furnace. The raw melting materials included DT4C pure iron, pure aluminum, pure nickel, and GCr15 bearing steel. It is noteworthy that the alloy was stirred uniformly under the action of the magnetic field. After the shell was formed by air cooling, the alloy, the billet of which had just become solidified, was impacted by a large amount of water (of about 20 °C temperature), and the metal was cooled to room temperature in a few minutes.

Table 1. Alloy chemical composition (in wt.%) determined by XRF (X-ray Fluorescence, 20°/min).

No.	Fe	Al	Cr	Ni	C	V	Ti
#1	72.27	7.91	13.17	6.65	-	-	-
#2	81.97	8.46	8.76	-	0.81	-	-
#3	75.15	12.25	10.29	2.11	0.20	-	-
#4	75.54	11.73	11.48	8.68	-	-	1.21
#5	82.57	8.80	4.86	2.19	-	1.36	-
#6	86.91	8.38	4.71	-	-	-	-

The grain morphology of the alloys was observed under a metallographic microscope, and their phase composition was analyzed by X-ray diffraction (XRD, D/mAX 2500, Japanese Neo-Confucianism Corporation, Tokyo, Japan). The surface morphology of the alloys was observed by field emission scanning electron microscopy (FESEM, JOEL JSM-7800F, Japan Electronics Corporation, Tokyo, Japan), and the main chemical components of the phases were analyzed by energy dispersive spectroscopy (EDS, JOEL JSM-7800F, Japan Electronics Corporation, Tokyo, Japan) coupled with FESEM. Subsequently, the as-cast alloys were cut into the specimens of 15 × 15 × 5 mm in size.

The #1, #2 and #3 alloys were heated from 20 to 1000 °C for 30 min, cooled by water (20 °C), re-heated to 1000 °C for 30 min, and then rolled by a rolling mill with a pair of work rolls under a rolling pressure of 25 T. The thickness of the samples was decreased from 5 to 2.5 mm during the rolling process. After rolling, the alloys were placed into a DHG-9053 thermal oven and dried at 200 °C for 72 h.

3. Results and Discussion

3.1. Second Phase of Alloys

From the metallographic observations, the matrix structure was divided into smaller grains by the second phase in #1, #2 and #3 alloys, and the matrix grains encountered the hindrance of the second phase during the growth process (Figures 1 and 2). Combining the EDS results (Table 2, Figures 3 and 4), it can be observed that the matrix structure was α-Fe solid solution of Fe_2AlCr. However, the second phases of the alloys with different compositions varied from each other. In particular, alloy #1 formed FeCr phase (σ phase), alloy #2 formed a mixed phase of FeCr phase and a great deal of carbide precipitation, and alloy #3 formed a mixed phase of FeCr and a little amount of carbide precipitation. In contrast, samples #4, #5, and #6 alloy did not have FeCr phase; they had a large grain size, which can reach several millimeters in diameter. The average rain diameter of each alloy was calculated by Image-pro software, #1 alloy's grain diameter was 86.7 µm, #2 alloy was 93.2 µm, #3 alloy was 95.5 µm, #4 alloy was 1035.3 µm, #5 was 4369.7 µm, and #6 was 3180.9 µm.

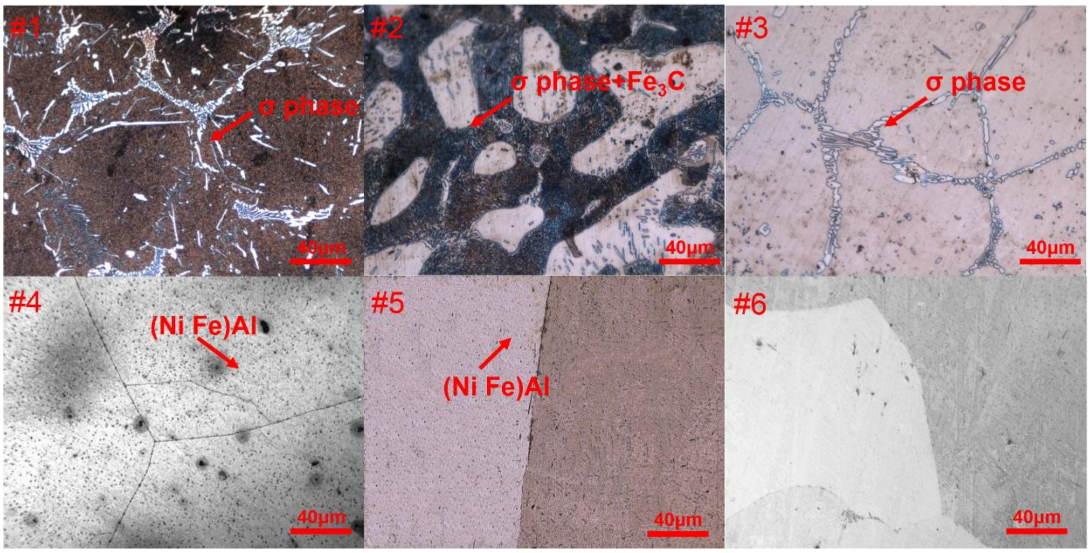

Figure 1. Metallography structure of alloys. FeCr phase appeared in #1, 2, and 3 alloys, (Ni Fe)Al appeared in #4 and #5 alloys. FeCr and (Ni Fe)Al's components are presented in Table 2.

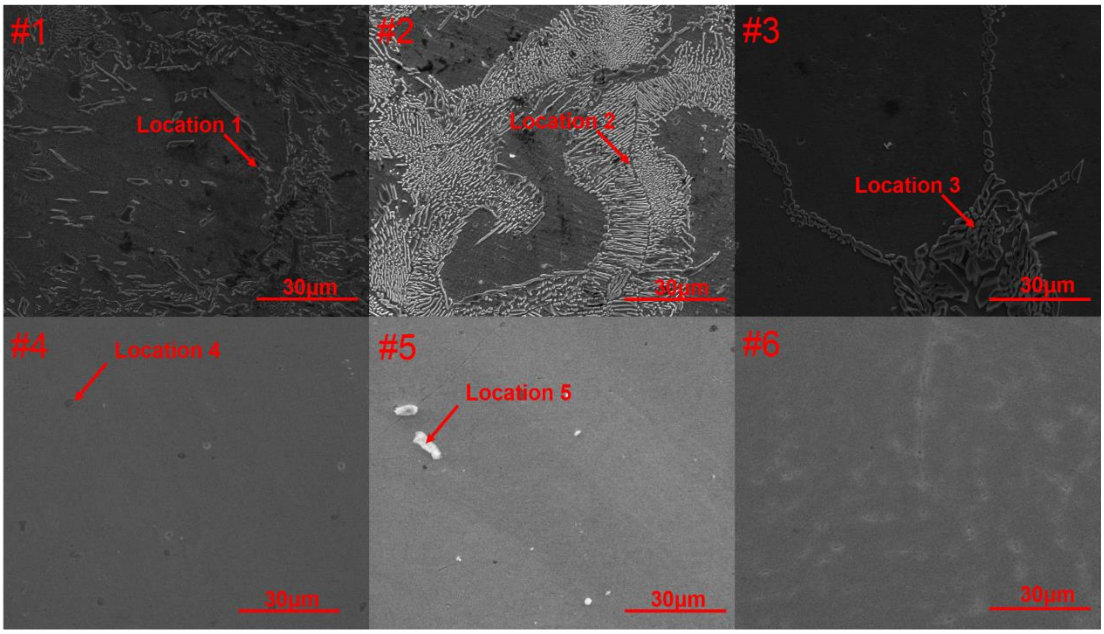

Figure 2. SEM image of alloys grain. A large number of FeCr phases accumulated at the grain boundaries in #1 alloy. In #2 alloy, FeCr phase nucleated on the carbide. There was distribution of FeCr along the grain boundary in 3# alloy. (Ni Fe)Al phase was precipitated in #4 and #5 alloys, which played the role of precipitation strengthening.

Table 2. Chemical compositions of the respective locations shown in Figure 2. There were both FeCr and carbides (Locations 1, 2 and 3), and there were (Ni Fe)Al in Locations 4 and 5.

Element	Location 1 (at. %)	Location 2 (at. %)	Location 3 (at. %)	Location 4 (at. %)	Location 5 (at. %)
Fe	53.64	57.68	59.72	73.19	75.86
Al	1.46	7.31	9.96	18.31	16.72
Cr	42.45	14.07	34.48	-	-
C	-	20.94	3.76	-	-
Ni	2.45	-	2.04	8.60	4.32

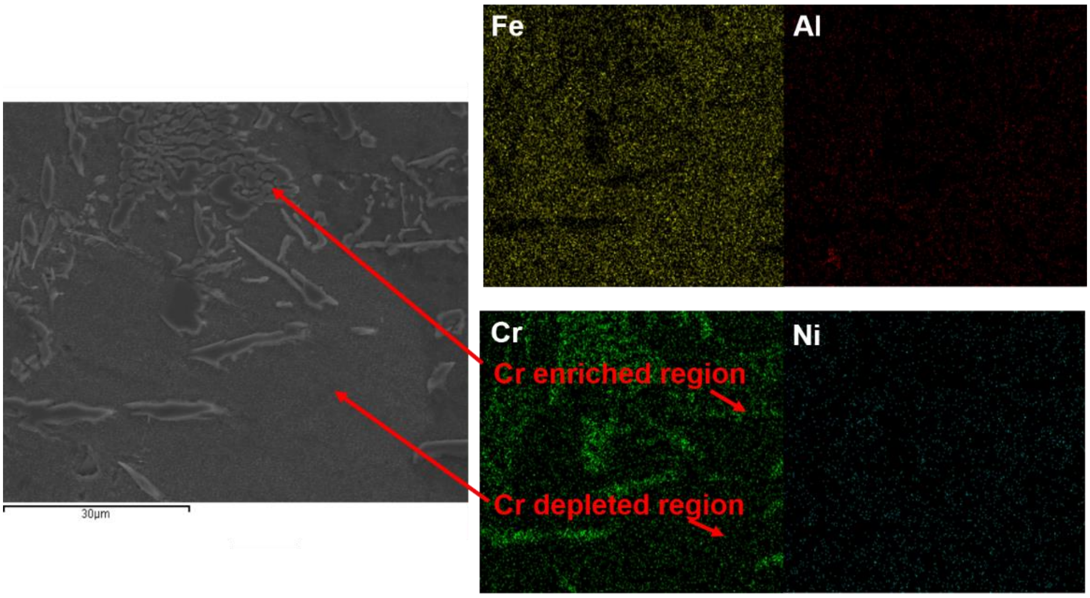

Figure 3. FESEM image of alloy #1, showing a sample grain and element distribution at a grain boundary. The distribution of elemental Cr is particularly important, as the distribution of elements coincides with that of phases.

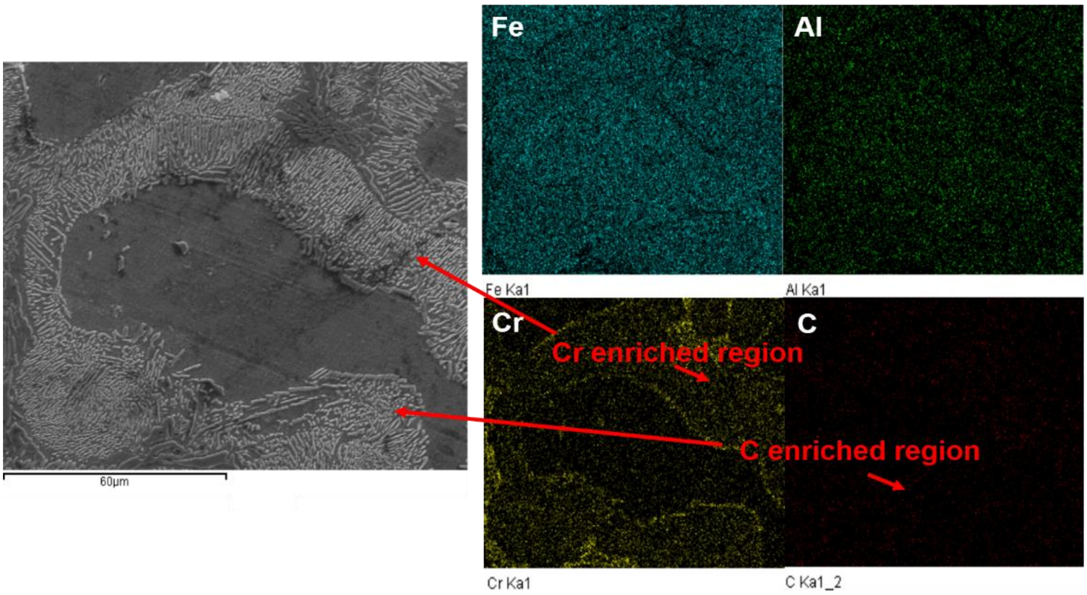

Figure 4. FESEM image of alloy #2 sample grain and element distribution at a grain boundary. The distribution of Cr elements coincides with that of the phases in the grain boundary.

There was no obvious grain boundary defect in the matrix in #1, #2 and #3 alloys' grain, whilst the second phase had an obvious grain boundary. The grain size of the matrix could reach tens of microns, whilst the grain size of the second phase was only a few microns. The second-phase grains were dendritic, a small portion of which were scattered in the matrix grains. The grain sizes of #4, #5 and #6 alloys reached hundreds of microns, and the alloys' grain boundaries were clean, without the second phase at the grain boundaries.

3.2. Thermodynamic Calculation

The matrix phase of Fe–Al–Cr alloys is ferrite structure, which is a body-centered cubic lattice. In our conception, we need to find a second phase of body-centered cubic crystal to meet two requirements. The second phase is needed to prevent the growth of ferrite grains, and to form a semi-eutectic lattice structure. σ phase is a destructive second phase in nickel-based superalloys, which is body-centered cubic crystal (its space group is Im3m (229)). The destructive effect of σ phase in nickel-based superalloys is that σ phase nucleates easily at grain boundaries and the lattice of nickel-based superalloys is usually a face-centered cubic structure [13].

σ phase is a kind of topological close-packed phase (TCP), which is easy to nucleate on grain boundaries and carbides. Thermodynamic calculation by FactSage6.2 (Equilib Module) shows that adding Ni element to the alloy is beneficial for the nucleation of σ phase (Figure 5) [14].

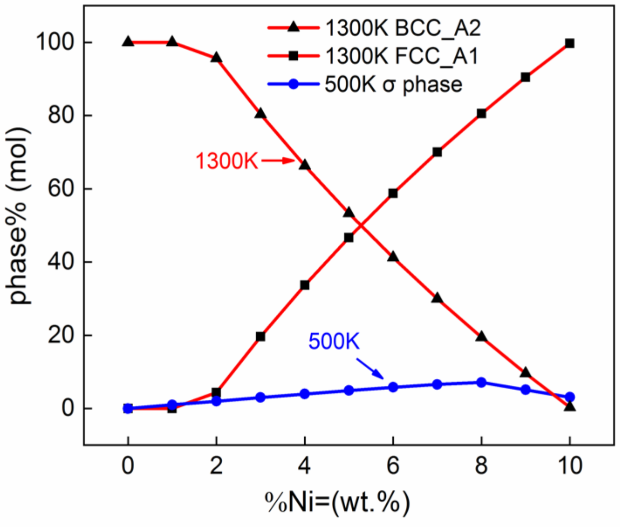

Figure 5. Relationship between Ni content in alloy and σ phase volume content in Fe-8 wt.%Cr-4 wt.% Al.

The nucleation of σ phase is related to the electron vacancy concentration in the lattice [15,16].

$$\triangle N_v = \overline{N}_v^c - \overline{N}_V \tag{1}$$

When $\triangle N_v$ is less than zero, σ phase will nucleate. The smaller $\triangle N_v$ is, the more σ phase will precipitate. $\overline{N}_v^c$ means critical electron vacancy and $\overline{N}_V$ means electrons vacancy density. Austenite's primary cell has higher electron vacancy density than ferrite. Thus, σ phase is easy to nucleate in austenite solid solution. Ni is a strong austenitic stabilization element, and a small amount of Ni can achieve stability austenitic phase (Figure 6). This explains the positive effect of Ni on σ phase nucleation.

Another reason is that the diffusion of Cr atoms in ferrite is easier than that in austenite. After alloy austenitizing, Cr atoms are confined to those regions and mixed with some free Fe atoms to form σ phase, which hinders the growth of Fe–Al–Cr alloy grains. Other austenitizing elements have similar effects with Ni elements, such as C (Figure 7). The effect of austenitizing on the second phase of the alloy is shown in Figure 5. Nickel equivalence has an important effect on austenitizing of alloys, and austenitizing affects the nucleation of FeCr.

The equilibrium multicomponent system has the smallest Gibbs free energy (Equation (1)). The thermodynamic description of a system requires that each phase has its corresponding thermodynamic function (Equation (2)), which is used to describe the relationship between temperature, pressure, concentration and various free energy functions. In the calculation of phase diagrams, Gibbs free energy of two-element phase in a multicomponent system can be decomposed into three independent parts (Equation (3)). The sub-lattice model is used for the ordered phase with ordered/disordered phase transition. The lattice position fraction occupied by atoms in the primary cell is used to replace the stoichiometric ratio in the solution model (Equations (4) and (5)).

$$G_{eq} = \min(\sum_{i=1}^{p} n_i G_i^{\Phi}) \tag{2}$$

$$G^{\Phi} = G_T^{\Phi}(T,x) + G_p^{\Phi}(p,T,x) + G_m^{\Phi}(T_c,\beta_0,T,x) \tag{3}$$

$$G^{\Phi} = x_A^0 G_A^0 + x_B^0 G_B^0 + \triangle G^f \tag{4}$$

$$x_A = a^1 y_A^1 + a^2 y_A^2 \tag{5}$$

$$x_B = a^1 y_B^1 + a^2 y_B^2 \tag{6}$$

The results of phase diagram calculation are as follows (Figures 6–8).

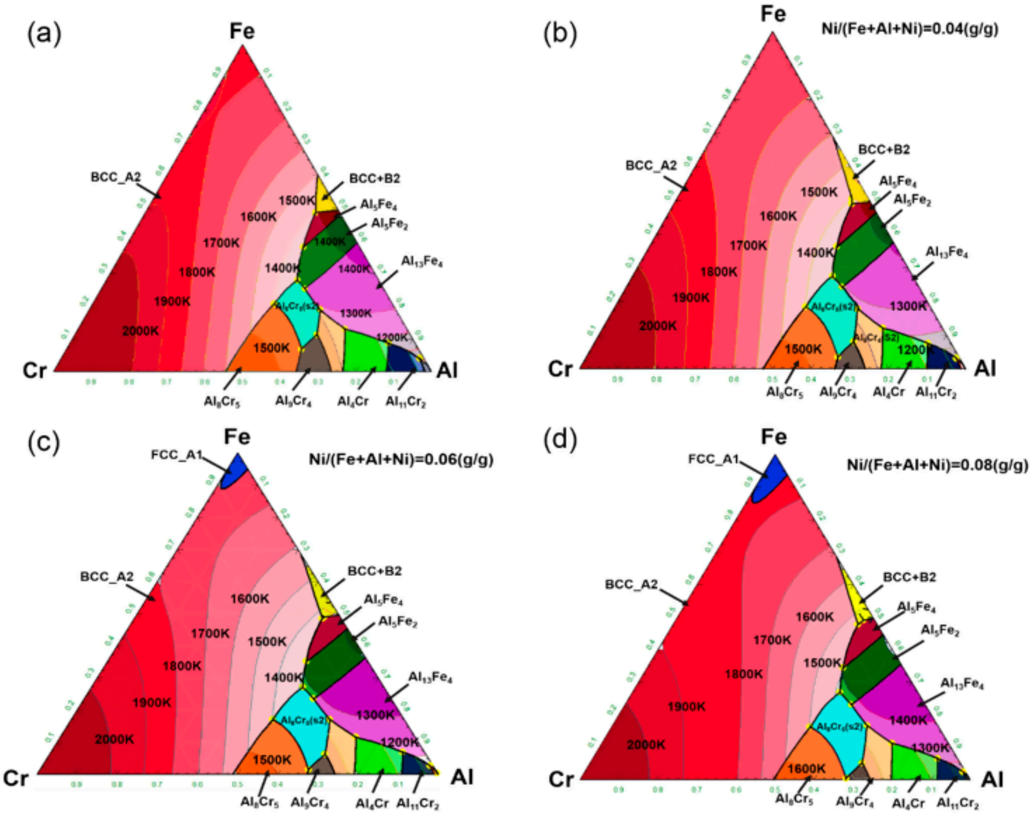

Figure 6. Effect of Ni addition on the Fe–Al–Cr phase diagram (1000–2000 K). (**a**) Ni/(Fe + Al + Cr) = 0 wt.%; (**b**) Ni/(Fe + Al + Cr) = 4 wt.%; (**c**) Ni/(Fe + Al + Cr) = 6 wt.%; and (**d**) Ni/(Fe + Al + Cr) = 8 wt.%.

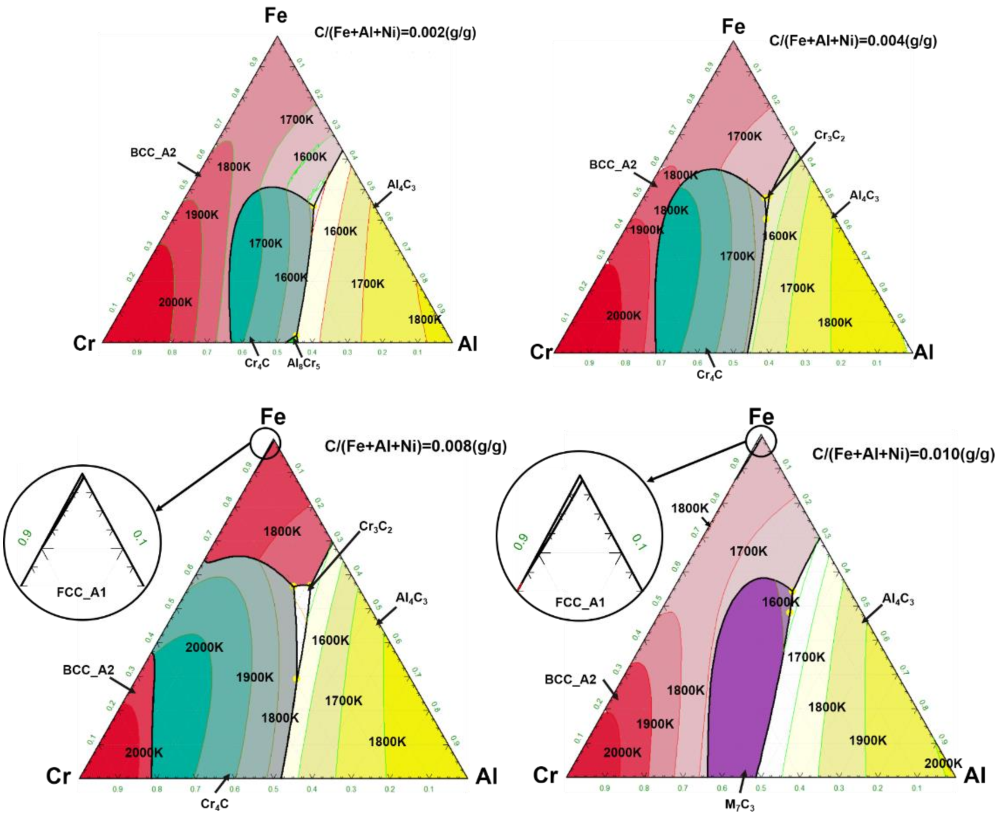

Figure 7. Effect of C addition on the Fe–Al–Cr phase diagram (1000–2000 K). (**a**) C/(Fe + Al + Cr) = 0.2 wt.%; (**b**) C/(F e+ Al + Cr) = 0.4 wt.%; (**c**) C/(Fe + Al + Cr) = 0.8 wt.%; and (**d**) C/(Fe + Al + Cr) = 1 wt.%.

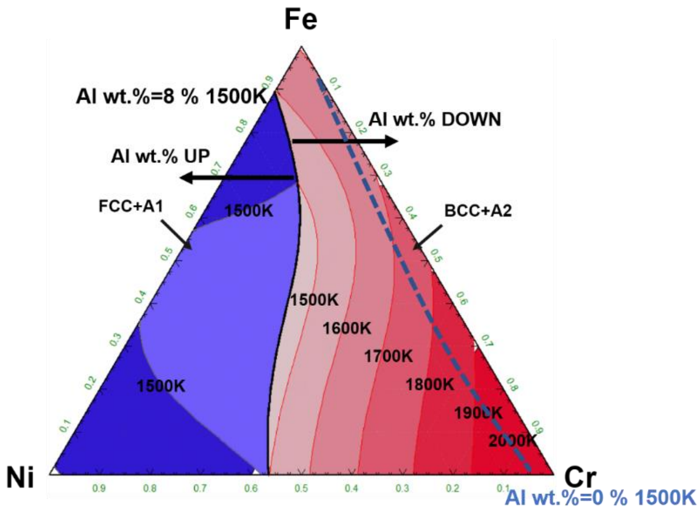

Figure 8. Effect of Al addition on the Fe–Ni–Cr phase diagram (1000–2000 K).

With the increase of aluminium content, the boundary between the austenite phase and the ferrite phase diagram shifts to the left until the austenite phase disappears completely. From Figure 9, austenitizing of Fe–Al–Cr alloys does not depend on the content of Ni, but on the ratio of Ni equivalent to Cr equivalent. This conclusion is confirmed by experiments (Figure 9). When the Ni/Cr ratio of alloys is more than 0.19, σ phase can nucleate in Fe–Al–Cr alloys.

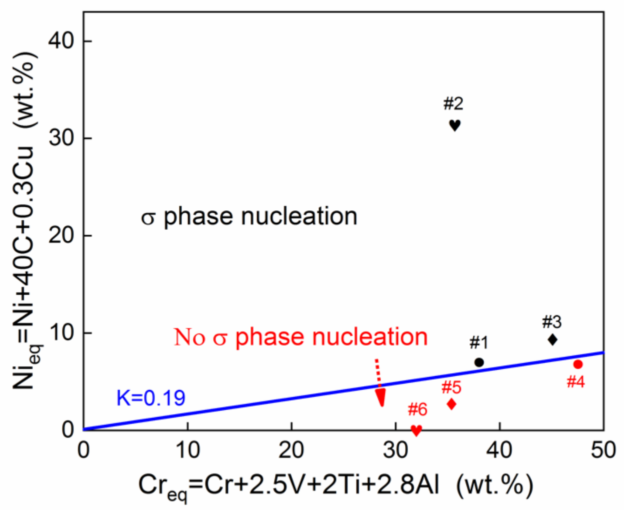

Figure 9. The different locations indicate the Cr/Ni ratio of the alloys.

3.3. *Effect of High Temperature Environment on σ Phase*

The matrix phase (Fe_2AlCr) of the alloys was coherent and coplanar with the second phase (FeCr). It was impossible to observe the behavior of the second phase at high temperature by XRD (Figure 10), because the matrix phase causes confusion. The effect of high temperature on phase A was studied using high temperature experiments.

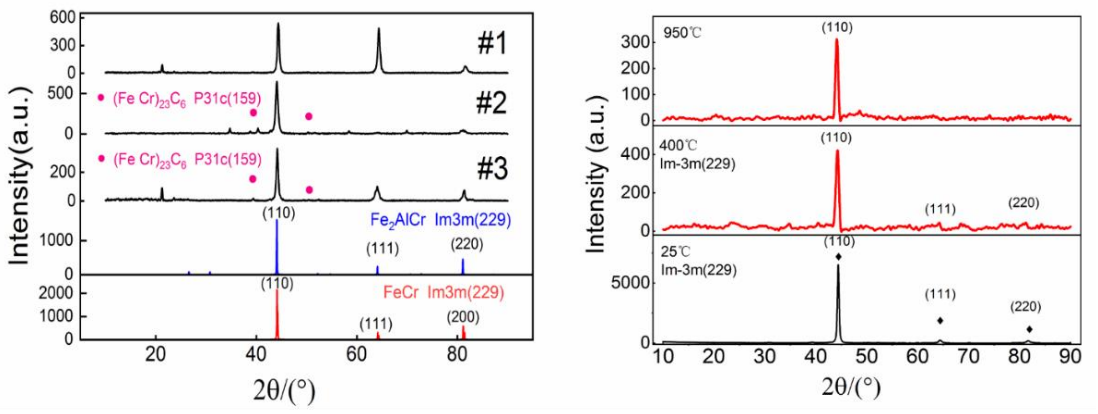

(a) **(b)**

Figure 10. XRD results of the #1, #2 and #3 alloys. (**a**) Comparison of XRD images of Alloys with XRD of Standard Substances. The Fe_2AlCr and FeCr phases were coherent and coplanar. (**b**) XRD results of #1 alloy at different temperatures.

The phase distribution and grain size around the grain boundary of the alloys was hardly changed by quenching. Thermomechanical treatment results (rolling) in obvious grain orientation: tangential direction of the deformation direction of the alloys. The grain size of the alloys tended to grow after aging at 200 °C for 72 h after deformation. In addition, the distribution of the second phase was significantly changed after thermomechanical treatment. The distribution became more dense and the grains became more chaotic whilst more second phase particles entered into the grains (Figure 11). Unfortunately, these heat treatments cannot refine the grain size of these alloys from the results. Moreover, after thermomechanical treatment, the toughness will be further decreased due to the formation of texture (Figure 12). In summary, thermomechanical treatment did not achieve the goal of grain refinement, which again indicated that the two phases are coherent and coplanar. σ phase will not decompose rapidly in a 1000 °C high temperature working environment, and it will not dissolve into the matrix in a short time heating process.

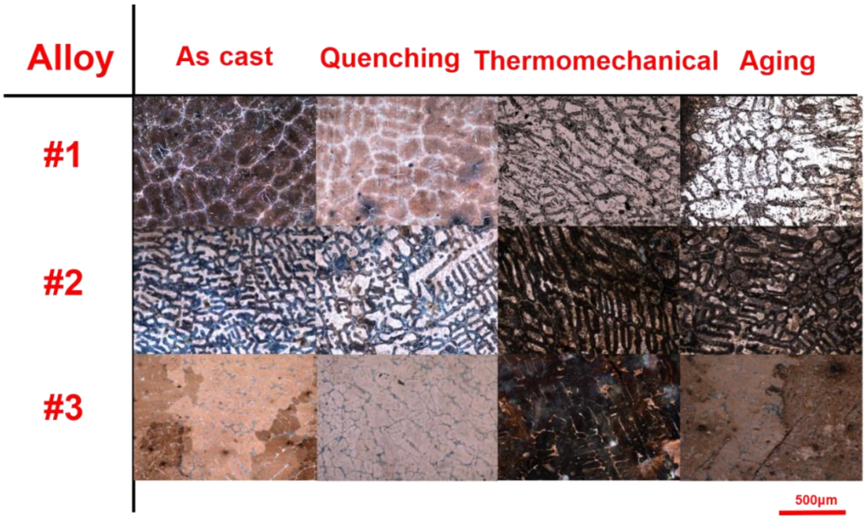

Figure 11. Metallographic structure changes in the four alloys during heat treatment. Alloys were heated from 20 to 1000 °C for 30 min, cooled by water (20 °C) re-heated to 1000 °C for 30 min, and after rolling, aging 72 h in 200 °C.

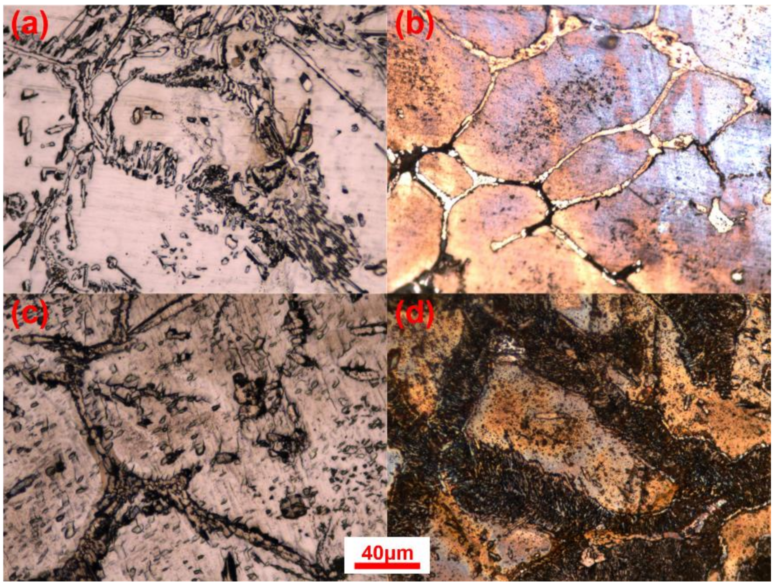

Figure 12. Alloy microstructure after a series of heat treatments. (**a**) Alloy #1; (**b**) alloy #2; (**c**) alloy #3; and (**d**) alloy #4.

4. Conclusions

(1) This study provides a new way for grain refinement of Fe–Al–Cr alloys and a new idea for commercial application on a large scale. In this study, FeCr(σ) phase was obtained in the Fe–Al–Cr alloys, which had grains of several microns and was coherent and coplanar with the matrix (Fe_2AlCr).

(2) σ phase nucleated in austenite. The nucleation of σ phase in Fe–Al–Cr alloys is controlled by the ratio of nickel to chromium. When the Ni/Cr (eq) ratio of alloys is more than 0.19, σ phase can nucleate in Fe–Al–Cr alloys.

(3) σ phase will not decompose rapidly in a 1000 °C high temperature working environment, and it will not dissolve into the matrix in a short time heating process.

Author Contributions: conceptualization, J.W.; methodology, S.L.; software, J.W.; validation, X.H.; formal analysis, J.W.; investigation, X.H.; resources, S.L.; data curation, J.W.; writing—original draft preparation, J.W.; writing—review and editing, J.W.; visualization, J.W.; supervision, J.W.; project administration, S.L.

Conflicts of Interest: The authors declare no conflict of interest.

References

1. Gregory, O.J.; Busch, E.; Fralick, G.C.; Chen, X. Preparation and characterization of ceramic thin film thermocouples. *Thin Solid Film* **2010**, *518*, 6093–6098. [CrossRef]
2. Deodeshmukh, V.P.; Matthews, S.J.; Klarstrom, D.L. High-temperature oxidation performance of a new alumina-forming Ni–Fe–Cr–Al alloy in flowing air. *Int. J. Hydrogen Energy* **2011**, *36*, 4580–4587. [CrossRef]
3. Stallybrass, C.; Schneider, A.; Sauthoff, G. The strengthening effect of (Ni, Fe)al precipitates on the mechanical properties at high temperatures of ferritic Fe–Al–Ni–Cr alloys. *Intermetallics* **2005**, *13*, 1263–1268. [CrossRef]
4. Stallybrass, C.; Sauthoff, G. Ferritic Fe–Al–Ni–Cr alloys with coherent precipitates for high-temperature applications. *Mater. Sci. Eng. A (Struct. Mater. Propert. Microstruct. Process.)* **2004**, *387–389*, 985–990. [CrossRef]
5. Sarkar, S.; Bansal, C. Atomic disorder–order phase transformation in nanocrystalline Fe–Al. *J. Alloys Compd.* **2002**, *334*, 135–142. [CrossRef]
6. Vo, N.Q.; Liebscher, C.H.; Rawlings, M.J.S.; Asta, M.; Dunand, D.C. Creep properties and microstructure of a precipitation-strengthened ferritic Fe–Al–Ni–Cr alloy. *Acta Mater.* **2014**, *71*, 89–99. [CrossRef]
7. Teng, Z.K.; Zhang, F.; Miller, M.K.; Liu, C.T.; Huang, S.; Chou, Y.T. Thermodynamic modeling and experimental validation of the Fe-Al-Ni-Cr-Mo alloy system. *Mater. Lett.* **2012**, *71*, 36–40. [CrossRef]
8. Liebscher, C.H.; Radmilovic, V.R.; Dahmen, U.; Vo, N.Q.; Dunand, D.C.; Asta, M.; Ghosh, G. A hierarchical microstructure due to chemical ordering in the bcc lattice: early stages of formation in a ferritic Fe–Al–Cr–Ni–Ti alloy. *Acta Mater.* **2015**, *92*, 220–232. [CrossRef]
9. Janda, D.; Ghassemiarmaki, H.; Bruder, E.; Hockauf, M.; Heilmaier, M.; Kumar, K.S. Effect of strain-rate on the deformation response of DO3-ordered Fe3Al. *Acta Mater.* **2016**, *103*, 909–918. [CrossRef]
10. Wang, J.; Han, X.; Liu, S.; Hou, W. Effects of Si and V on high temperature oxidation resistance of Fe-Al-Cr alloys. *J. Chongqing Univ.* **2019**, *42*, 86–97.
11. Minamino, Y.; Koizum, Y.; Tsuji, N.; Hirohata, N.; Mizuuchi, K.; Ohkanda, Y. Microstructures and mechanical properties of bulk nanocrystalline Fe–Al–C alloys made by mechanically alloying with subsequent spark plasma sintering. *Sci. Technol. Adv. Mater.* **2004**, *5*, 133–143. [CrossRef]
12. Risanti, D.D.; Sauthoff, G. Strengthening of iron aluminide alloys by atomic ordering and Laves phase precipitation for high-temperature applications. *Intermetallics* **2005**, *13*, 1313–1321. [CrossRef]
13. Palm, M.; Sauthoff, G. Deformation behaviour and oxidation resistance of single-phase and two-phase L21-ordered Fe–Al–Ti alloys. *Intermetallics* **2004**, *12*, 1345–1359. [CrossRef]
14. Ha, M.C.; Koo, J.M.; Lee, J.K.; Hwang, S.W.; Park, K.T. Tensile deformation of a low density Fe–27Mn–12Al–0.8C duplex steel in association with ordered phases at ambient temperature. *Mater. Sci. Eng. A* **2013**, *586*, 276–283. [CrossRef]
15. Zhao, X.B.; Dang, Y.Y.; Yin, H.F.; Lu, J.T.; Yuan, Y.; Cui, C.Y.; Gu, Y.F. Super-supercritical power stations with nickel-iron-based high-temperature alloy TCP phase and carbide precipitation thermodynamic calculations. *Mater. Eng.* **2015**, *43*, 38–43.
16. Baik, S.I.; Rawlings, M.J.S.; Dunand, D.C. Atom probe tomography study of Fe-Ni-Al-Cr-Ti ferritic steels with hierarchically-structured precipitates. *Acta Mater.* **2018**, *144*, 707–715. [CrossRef]